



Deposited via The University of Sheffield.

White Rose Research Online URL for this paper:

<https://eprints.whiterose.ac.uk/id/eprint/133831/>

Version: Accepted Version

---

**Article:**

Panyasantisuk, J., Dall'Ara, E., Pretterklieber, M. et al. (2018) Mapping anisotropy improves QCT-based finite element estimation of hip strength in pooled stance and side-fall load configurations. *Medical Engineering and Physics*, 59. pp. 36-42. ISSN: 1350-4533

<https://doi.org/10.1016/j.medengphy.2018.06.004>

---

© 2018 Elsevier. This is an author produced version of a paper subsequently published in *Medical Engineering & Physics*. Uploaded in accordance with the publisher's self-archiving policy. Article available under the terms of the CC-BY-NC-ND licence (<https://creativecommons.org/licenses/by-nc-nd/4.0/>).

**Reuse**

This article is distributed under the terms of the Creative Commons Attribution-NonCommercial-NoDerivs (CC BY-NC-ND) licence. This licence only allows you to download this work and share it with others as long as you credit the authors, but you can't change the article in any way or use it commercially. More information and the full terms of the licence here: <https://creativecommons.org/licenses/>

**Takedown**

If you consider content in White Rose Research Online to be in breach of UK law, please notify us by emailing [eprints@whiterose.ac.uk](mailto:eprints@whiterose.ac.uk) including the URL of the record and the reason for the withdrawal request.



# Mapping anisotropy improves QCT-based finite element estimation of hip strength in pooled stance and side-fall load configurations

J. Panyasantisuk<sup>a</sup>, E. Dall'Ara<sup>b</sup>, M. Pretterklieber<sup>c</sup>, D. H. Pahr<sup>d</sup>, P. K. Zysset<sup>a,\*</sup>

<sup>a</sup>*Institute for Surgical Technology and Biomechanics, University of Bern, Switzerland*

<sup>b</sup>*Department of Oncology and Metabolism and INSIGNEO, Institute for in silico Medicine, University of Sheffield, United Kingdom*

<sup>c</sup>*Division of Anatomy, Medical University of Vienna, Austria*

<sup>d</sup>*Institute for Lightweight Design and Structural Biomechanics, Vienna University of Technology and Department for Anatomy and Biomechanics, Karl Landsteiner Private University for Health Sciences, Austria*

---

## Abstract

Hip fractures are one of the most severe consequences of osteoporosis. Compared to the clinical standard of DXA-based aBMD at the femoral neck, QCT-based FEA delivers a better surrogate of femoral strength and gains acceptance for the calculation of hip fracture risk when a CT reconstruction is available. Isotropic, homogenised voxel-based, finite element (hvFE) models are widely used to estimate femoral strength in cross-sectional and longitudinal clinical studies. However, fabric anisotropy is a classical feature of the architecture of the proximal femur and the second determinant of the homogenised mechanical properties of trabecular bone. Due to the limited resolution, fabric anisotropy cannot be derived from clinical CT reconstruc-

---

\*Corresponding author

*Email address:* philippe.zysset@istb.unibe.ch (P. K. Zysset)

tions. Alternatively, fabric anisotropy can be extracted from HR-pQCT images of cadaveric femora. In this study, fabric anisotropy from HR-pQCT images was mapped onto QCT-based hvFE models of 71 human proximal femora for which both HR-pQCT and QCT images were available. Stiffness and ultimate load computed from anisotropic hvFE models were compared with previous biomechanical tests in both stance and side-fall configurations. The influence of using the femur-specific versus a mean fabric distribution on the hvFE predictions was assessed. Femur-specific and mean fabric enhance the prediction of experimental ultimate force for the pooled, i.e. stance and side-fall, (isotropic:  $r^2=0.81$ , femur-specific fabric:  $r^2=0.88$ , mean fabric:  $r^2=0.86$ ,  $p < 0.001$ ) but not for the individual configurations. Fabric anisotropy significantly improves bone strength prediction for the pooled configurations, and mapped fabric provides a comparable prediction to true fabric. The mapping of fabric anisotropy is therefore expected to help generate more accurate QCT-based hvFE models of the proximal femur for personalised or multiple load configurations.

*Keywords:* anisotropy, fabric, finite element analysis, proximal femur, quantitative computed tomography, bone strength

---

Number of words: 3916

## 1. Introduction

Hip fractures lead to mortality, morbidity and high health care costs. The effective prevention of hip fractures requires an accurate diagnosis of osteoporosis, which is currently based on measurement of areal bone mineral density (aBMD) measured by dual energy x-ray absorptiometry (DXA). However, the majority of fractures occur in patients with aBMD above the diagnostic threshold [1, 2, 3]. This reflects the fact that aBMD alone has high specificity but low sensitivity. Alternatively, Kopperdahl et al. [4] defined femoral strength thresholds, which were based on finite element (FE) analysis, equivalent to aBMD diagnostic criterion. Based on clinical data, a combination of FE-based femoral strength and aBMD identified more individuals at high fracture risk than aBMD alone [4]. FE analysis was also shown to estimate the failure load more accurately than radiography, DXA or quantitative computed tomography (QCT) [5]. FE approaches based on computer tomography (CT) have been applied extensively throughout the past decades to simulate the mechanical behaviour of the proximal femur [6, 7, 8, 9, 10, 11, 12, 13, 14, 15, 16, 17]. With availability of quantitative CT (QCT) in hospitals, QCT-based FE analyses have been increasingly included in hip studies and clinical evaluation of drug treatments against osteoporosis [18, 19]. To evaluate the ability in predicting bone strength, QCT-based FE models of the proximal femur were validated based on mechanical tests in which proximal femora were tested in the one-legged stance [20, 21, 22, 23, 24] or unprotected side-fall configuration [25, 26, 10, 27, 14, 17]. To a lesser ex-

24 tent, QCT-based FE models of the proximal femur were validated in both  
25 configurations [28, 12, 29, 5].

26 Homogenised, voxel-based FE (hvFE) models can be generated by con-  
27 verting re-coarsened QCT image voxels to hexahedral cubic elements. A  
28 homogenised material property is assigned to each element that is based  
29 on a statistically representative volume element (RVE) of the material [30].  
30 Homogenised elastic and yield properties are best predicted by bone vol-  
31 ume fraction (BV/TV) and fabric anisotropy of trabecular bone [31, 32],  
32 but QCT images are lacking information on trabecular microstructure due  
33 to the limited resolution. Therefore, bone is usually assumed to behave  
34 isotropically in QCT-based FE models of the proximal femur [33]. Several  
35 approaches were proposed to extract fabric tensors from QCT images, but  
36 fabric anisotropy cannot be derived accurately [34, 35, 36]. On the other  
37 hand, anisotropic homogenised FE models based on high resolution periph-  
38 eral QCT (HR-pQCT) improved the prediction of stiffness [11] and experi-  
39 mental bone strength [37, 13]. Enns-Bray et al. [14, 15] proposed a method  
40 to map femoral anisotropy from HR-pQCT into QCT-based FE models by  
41 using the direct mechanics [38] and then the mean intercept length (MIL)  
42 method [39, 40]. However, both studies involved only linear FE analyses  
43 of the proximal femur in a single load configuration. Little is known about  
44 the effect of including HR-pQCT derived fabric anisotropy into QCT-based,  
45 geometrically and materially non-linear hvFE of the human proximal femur  
46 in different loading configurations.

47       Alternatively, trabecular fabric anisotropy can be estimated from the HR-  
48 pQCT image of a dissected femur with multiple approaches [41, 42, 43, 44,  
49 45]. Taghizadeh et al. [45] showed that averaged fabric anisotropy is a close  
50 approximation of patient-specific anisotropy and can be used in FE models.  
51 Chandran et al. [46] used a more systematic approach by selecting a mean  
52 femur with the closest shape and intensity to the femurs of a database (n=71).  
53 To our best knowledge, none of aforementioned approaches were tested for  
54 QCT-based hvFE models. We employed the latter single-template approach  
55 to obtain the natural fabric distribution of a mean human proximal femur  
56 and to build anisotropic hvFE models using CT scans of clinical quality. In  
57 this study, fabric anisotropy from the HR-pQCT images of the femur-specific  
58 and the mean femur were mapped to QCT-based hvFE models and non-linear  
59 FE analyses were performed to compute stiffness and strength.

60       The goal of this study was to assess the effect of including femur-specific  
61 or mean fabric anisotropy on the predictive ability of non-linear QCT-based  
62 hvFE models of the human proximal femur, as compared with experimentally  
63 measured stiffness and strength in two loading configurations.

## 64 **2. Materials and methods**

65       Seventy-two human proximal femora (35 males, 37 females, age  $77\pm 11$   
66 years, range 46-96 years) were obtained from body donors prepared by the  
67 Division of Anatomy of the Medical University of Vienna. Collection and  
68 preparation procedures were approved by the ethics commission of the Medi-

69 cal University of Vienna. Informed consent was obtained from all donors.  
70 Sample preparation, imaging and mechanical testing of femora were ex-  
71 plained in detail by [12] and [13]. According to the calculated T-score from  
72 DXA, 29 of the femora were osteoporotic, 22 were osteopenic and 21 were  
73 normal. The procedures are explained here briefly.

#### 74 *2.1. Imaging and testing*

##### 75 *QCT scanning*

76 Each femur was scanned with a clinical QCT (Brilliance 64, Philips, Ger-  
77 many; intensity: 100 mA; voltage: 120 kV; voxelsize:  $0.33 \times 0.33 \times 1.0 \text{ mm}^3$ )  
78 with a calibration phantom (BDC phantom, QMR GmbH, Germany) for con-  
79 verting the Hounsfield unit (HU) scale to equivalent BMD scale in mgHA/CC.  
80 The BMD range was restricted to -100 and 1400 mgHA/cc to decrease the  
81 effect of residual air bubbles and other artefacts [12].

##### 82 *HR-pQCT scanning*

83 Each femur was also scanned with an HR-pQCT (Xtreme CT, Scanco, Switzer-  
84 land; intensity: 900  $\mu\text{A}$ , voltage: 60 kVp, voxel size:  $0.082 \times 0.082 \times 0.082$   
85  $\text{mm}^3$ ). The scanned images were converted from HU to BMD scale following  
86 the manufacturer's calibration procedure. Similarly to QCT, the BMD range  
87 was restricted to -100 and 1400 mgHA/cc [13].

##### 88 *Mechanical tests*

89 A femur of each pair was randomly selected to be tested in a one-legged

90 stance and side-fall configuration. In stance configuration, the cranial por-  
91 tion of the femoral head was embedded in polyurethane (PU). In side-fall  
92 configuration, the medial portion of the femoral head and the lateral por-  
93 tion of the greater trochanter were embedded in PU. The shaft was fixed in  
94 both configurations. A custom-made bearing was used to reduce transverse  
95 forces/moments by allowing rotation and 2 translations perpendicular to the  
96 loading axis. Each femur was compressed to failure by a servo-hydraulic  
97 testing machine (Mini-Bionix, MTS system, USA) at a rate of 5 mm/min.  
98 Femoral ultimate force was defined as the maximum compressive load. The  
99 stiffness was the maximum slope of the linear part of the load-displacement  
100 curve [12].

## 101 *2.2. QCT-based hvFE model generation*

102 The QCT images of the femora were cropped proximally, upsampled along  
103 the scanning axis to isotropic voxel size of 0.33 mm, rotated to an experi-  
104 mental position (stance or side-fall configuration), masked and coarsened to  
105 a resolution of 3 mm. A filling out algorithm was used to find the outer  
106 contour of each image. Image processing was done with the software MED-  
107 TOOL ([www.dr-pahr.at](http://www.dr-pahr.at)). Due to the equivalent performance of voxel and  
108 smooth mesh FE models in a recent QCT-based clinical study [47], it was  
109 decided to use the simpler voxel mesh in this study. An hvFE model of each  
110 femur was therefore generated by converting image voxels to linear hexahe-  
111 dron elements. Each voxel was assigned its local voxel BMD values. The

112 calibration relationship between BMD and BV/TV is provided in Dall’Ara  
113 et al. [12].

#### 114 *Image registration*

115 Grayscale HR-pQCT images were segmented in the original coordinate sys-  
116 tem with the manufacturer’s software (Scanco Medical, Switzerland). Both  
117 grayscale and segmented HR-pQCT images were pre-oriented (left/right and  
118 top/bottom) along the experimental position by using the flipping function in  
119 MIPAV software (<http://mipav.cit.nih.gov>). Rotated QCT images were up-  
120 sampled to 82  $\mu\text{m}$  isotropic voxels. In the following description of the image  
121 registration methodology, HR-pQCT and QCT images refer to pre-oriented  
122 HR-pQCT and upsampled rotated QCT images, respectively.

123 A mean femur closest to all the femurs of the available collection was  
124 selected. To do so, each donor femur image was registered to all the femora  
125 to quantify the distance metric based on the logarithm of the left stretch  
126 tensor of the gradient of the non-rigid transformation [46]. Based on this  
127 calculation, the femur with the minimal cumulated distance metric to all  
128 other femora was chosen to be the mean femur, which was then excluded  
129 from the analysis. Therefore, the femur dataset included the remaining 71  
130 femora. Subsequently, image registrations were performed by using the soft-  
131 ware ELASTIX [48] to calculate two types of transformations.

1. A donor femur transformation  $\mathbf{t}_o$  is a rigid transformation which maps  
coordinates in an HR-pQCT image ( $\mathbf{x}_{\text{HRpQCT}_{\text{donor}}}$ ) to coordinates in the

QCT image ( $\mathbf{x}_{\text{QCT}_{\text{donor}}}$ ) of the same donor. The expression is defined as:

$$\mathbf{x}_{\text{QCT}_{\text{donor}}} = \mathbf{t}_o(\mathbf{x}_{\text{HRpQCT}_{\text{donor}}}) = \mathbf{R}_o(\mathbf{x}_{\text{HRpQCT}_{\text{donor}}} - \mathbf{c}_o - \mathbf{b}_o) + \mathbf{c}_o \quad (1)$$

132 where  $\mathbf{R}_o$ ,  $\mathbf{c}_o$ ,  $\mathbf{b}_o$  are the rotation matrix, the centre of rotation and the  
 133 translation vector, respectively.

134 2. A mean-femur transformation  $\mathbf{t}_m$  combined two-step transformations  
 135 from the mean-femur HR-pQCT image to a donor QCT image. First,  
 136 the transformation  $\mathbf{t}_{m_1}$  is a rigid transformation which maps coordi-  
 137 nates in the mean-femur HR-pQCT image ( $\mathbf{x}_{\text{HRpQCT}_{\text{mean}}}$ ) to coordinates  
 138 in the mean-femur QCT image ( $\mathbf{x}_{\text{QCT}_{\text{mean}}}$ ). The expression is given by:

$$\mathbf{x}_{\text{QCT}_{\text{mean}}} = \mathbf{t}_{m_1}(\mathbf{x}_{\text{HRpQCT}_{\text{mean}}}) = \mathbf{R}_{m_1}(\mathbf{x}_{\text{HRpQCT}_{\text{mean}}} - \mathbf{c}_{m_1} - \mathbf{b}_{m_1}) + \mathbf{c}_{m_1} \quad (2)$$

139 where  $\mathbf{R}_{m_1}$ ,  $\mathbf{c}_{m_1}$ ,  $\mathbf{b}_{m_1}$  were the rotation matrix, the centre of rotation  
 140 and the translation vector, respectively.

141 Second, the transformation  $\mathbf{t}_{m_2}$  combines rigid and non-rigid (affine and  
 142 b-spline) transformations from  $\mathbf{x}_{\text{QCT}_{\text{mean}}}$  to  $\mathbf{x}_{\text{QCT}_{\text{donor}}}$ . The expression  
 143 is given by:

$$\mathbf{x}_{\text{QCT}_{\text{donor}}} = \mathbf{t}_{m_2}(\mathbf{x}_{\text{QCT}_{\text{mean}}}) = \mathbf{t}_B(\mathbf{t}_A(\mathbf{t}_R(\mathbf{x}_{\text{QCT}_{\text{mean}}})) \quad (3)$$

144 where  $\mathbf{t}_B$ ,  $\mathbf{t}_A$  and  $\mathbf{t}_R$  denote b-spline, affine, and rigid transformations,

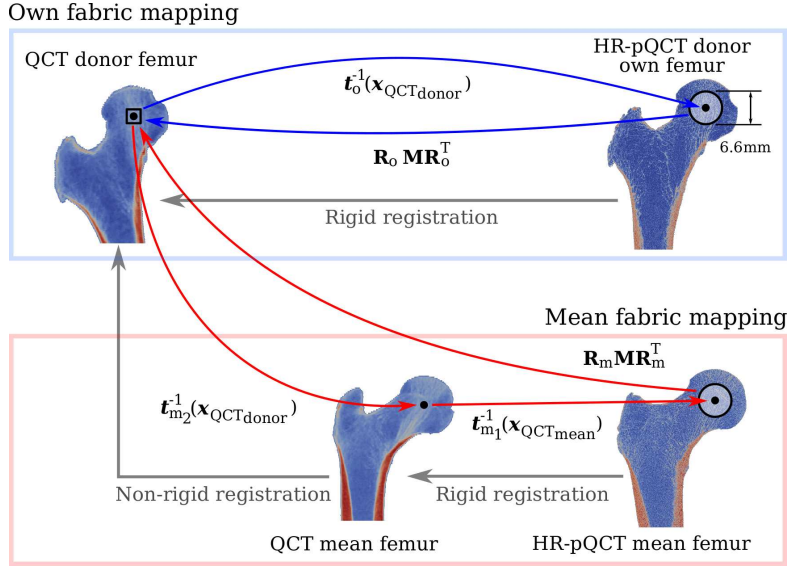


Figure 1: Fabric mapping methodology for femur-specific and mean femur HR-pQCT images.  $\mathbf{t}_o^{-1}$ ,  $\mathbf{t}_{m_1}^{-1}$  and  $\mathbf{t}_{m_2}^{-1}$  are transformations from donor QCT to donor HR-pQCT, from mean-femur QCT to mean-femur HR-pQCT and from donor QCT to mean-femur QCT image.  $\mathbf{M}$  is a fabric tensor.  $\mathbf{R}_o$  and  $\mathbf{R}_m$  are rotation matrices from donor HR-pQCT to donor QCT and from mean-femur HR-pQCT to donor QCT image.

145

respectively.

Finally, the total mean-femur transformation  $\mathbf{t}_m$  is expressed as:

$$\mathbf{x}_{\text{QCT}_{\text{donor}}} = \mathbf{t}_m(\mathbf{x}_{\text{HRpQCT}_{\text{mean}}}) = \mathbf{t}_{m_2}(\mathbf{t}_{m_1}(\mathbf{x}_{\text{HRpQCT}_{\text{mean}}})) \quad (4)$$

146 *Fabric mapping*

147 Figure 1 shows the fabric mapping methodology for donor femora and mean  
148 femora. Fabric mapping was then performed for QCT images with 3 mm  
149 mesh size. For femur-specific fabric mapping,  $\mathbf{x}_{\text{QCT}_{\text{donor}}}$  were mapped to  
150  $\mathbf{x}_{\text{HRpQCT}_{\text{donor}}}$  by using the transformation  $\mathbf{t}_o^{-1}$ . For mean fabric mapping,  
151  $\mathbf{x}_{\text{QCT}_{\text{donor}}}$  were mapped to  $\mathbf{x}_{\text{QCT}_{\text{mean}}}$  by using the transformation  $\mathbf{t}_{m_2}^{-1}$  and  
152  $\mathbf{x}_{\text{QCT}_{\text{mean}}}$  were mapped to  $\mathbf{x}_{\text{HRpQCT}_{\text{mean}}}$  by using the transformation  $\mathbf{t}_{m_1}^{-1}$ . In  
153 the HR-pQCT image, a fabric tensor was calculated over a spherical RVE  
154 by using the MIL method. The spherical RVE had a diameter of 6.6 mm  
155 which had the same volume as a cube with 5.3 mm edge length used in  
156 trabecular bone homogenisation [49, 50, 51]. Then, the fabric tensor was  
157 rotated back to the coordinate system of the donor QCT image by using  $\mathbf{R}_o$   
158 for the femur-specific fabric mapping and  $\mathbf{R}_m$  for the mean fabric mapping,  
159 where  $\mathbf{R}_m = \mathbf{R}_{m_2}\mathbf{R}_{m_1}$  and  $\mathbf{R}_{m_2}$  was the rotation matrix derived from the  
160 polar decomposition  $\mathbf{R}\mathbf{U}$  of the gradient of the transformation  $\mathbf{t}_{m_2}$  [52].

161 *Embedding and FE model generation*

162 A PU and a steel layer of cylindrical shape were modelled as in the exper-  
163 imental setup shown in Fig. 2. hvFE models of the proximal femur were  
164 generated by converting image down-sampled voxels ( $3 \text{ mm}^3$ ) to hexahedral  
165 cubic elements.

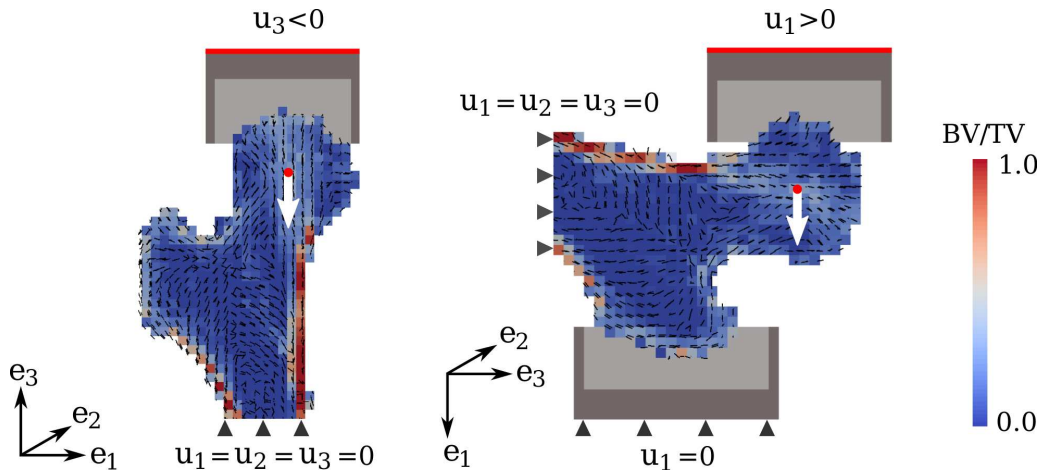


Figure 2: Homogenised voxel FE models in stance and side-fall configurations. The principle direction of mean fabric tensors is illustrated by small black lines.  $u_i$  and  $e_i$  are displacements and unit directions. The displacement was applied on the reference node at the centre of the femoral head (red dot) which was coupled with the embedding boundary (red line).

166 *Boundary conditions*

167 The boundary conditions were improved with respect to the original FE  
 168 analyses of Dall’Ara et al. [12]. The lever arm of the applied force was main-  
 169 tained in the centre of the femoral head to account for the motion between  
 170 the loading cup and the articular cartilage. The radius of each femoral head  
 171 was computed by fitting a sphere to the femoral head using BoneJ, a plugin in  
 172 ImageJ [53, 54]. A reference node at the center of the femoral head was kine-  
 173 matically coupled with the top surface of the loading cups and constrained  
 174 with a displacement in the loading direction only. In-plane translations and  
 175 rotations were left free to simulate the experimental setup. In side-fall con-  
 176 figuration, the most lateral surface of the steel embedding below the greater  
 177 trochanter was fixed only in the loading direction. In both configurations,

Table 1: Elasticity and strength model parameters

Variable Unit	Elasticity					Strength		
	$\varepsilon_0$ [MPa]	$\nu_0$ [-]	$\mu_0$ [MPa]	$k$ [-]	$l$ [-]	$\sigma_0$ [MPa]	$\chi_0$ [-]	$\tau_0$ [MPa]
Tension (+)	6614	0.246	2654	1.33	1.0	54.8	-0.246	44.6
Compression (-)						72.9	0.333	

178 the distal surface of the shaft was fixed in all directions.

179 *Material properties*

180 The material properties of the embedding were assumed isotropic with Pois-  
181 son ratio 0.3. PU elements were assigned Young’s modulus 1.36 GPa and  
182 steel elements 210 GPa. The elastic-damage constitutive law was adapted  
183 from [55] which includes volume fraction and fabric-based elasticity [56] and  
184 a piecewise Hill yield criterion [57]. Table 1 shows the anisotropic material  
185 constants taken from [58] and applied to the axial compression of vertebral  
186 body sections in [59]. The material properties of cortical bone were extrap-  
187 olated from those of trabecular bone by using a nonlinear but smooth tissue  
188 function [12]. At  $BV/TV = 1$ , the elastic modulus equals 24 GPa, the com-  
189 pressive strength 266 MPa and the tensile strength equals 200 MPa. An  
190 exponential hardening law was applied. The damage variable is an exponen-  
191 tial function of the cumulated plastic strain and represents the progressive  
192 failure of the bone element and ranges from 0 (intact) to 1 (failed) [55].

193 *FE analyses*

194 Nonlinear FE analyses were performed by using Abaqus (Abaqus 2016, Simu-  
195 lia, Dassault Systemes, Velizy-Villacoublay, France) until the maximum dis-  
196 placement was reached. FE stiffness was defined as the slope in the first steps  
197 and ultimate load as the maximum force in the force-displacement curve. The  
198 damage variable was computed in each element at every step.

199 Linear regressions of the relationship between computed and experimental  
200 results (i.e. ultimate force and stiffness) of pooled (combined stance and  
201 side-fall) configurations and the two individual load configurations were cal-  
202 culated for comparison. The significance level was set to  $p < 0.05$  and the  
203 correlation coefficients  $r^2$  were compared by using William's formula [60].

### 204 **3. Results**

205 Fabric anisotropy significantly improved the prediction of experimental  
206 ultimate force in pooled configurations. Correlation  $r^2$  between hvFE and  
207 experimental ultimate force increased from 0.81 to 0.88 ( $p < 0.001$ ) for femur-  
208 specific fabric and to 0.86 ( $p < 0.001$ ) for mean fabric (Table 2). Prediction  
209 of isotropic hvFE models were equivalent to hvFE models from Dall'Ara  
210 et al. [12]. In single load configurations, anisotropy did not improve the  
211 predictions (stance:  $r^2$  from 0.82 to 0.84 with  $p = 0.1$ ). Regression lines of  
212 anisotropic models were closer to the 1:1 line compared to isotropic models  
213 (isotropic:  $y = 1.6x - 0.369$ , femur-specific fabric:  $y = 1.1x + 0.134$ , mean  
214 fabric:  $y = 1.2x + 0.388$ ). Table 3 shows the correlation coefficients  $r^2$

Table 2: **Prediction of ultimate force.** Coefficients of determination  $r^2$  and standard errors of the estimate ( $SEE$ ) of the linear regressions of the relationships between hvFE and experimental ultimate force in pooled stance and side-fall configurations, stance configuration and side-fall configuration. Comparison was made with previous studies on the same collection of femora.

	$r^2$			$SEE$ [kN]		
	pooled	stance	fall	pooled	stance	fall
<b>QCT [12]</b>						
Isotropic	0.80	0.80	0.85	1.58	1.28	0.44
<b>QCT Present study</b>						
Isotropic	0.81	0.82	0.87	1.58	1.32	0.41
Anisotropic: mean fabric	0.86	0.80	0.85	1.33	1.31	0.44
Anisotropic: femur-specific fabric	0.88	0.84	0.86	1.22	1.15	0.42
<b>HR-pQCT [13]</b>						
Anisotropic: femur-specific fabric	0.88	0.87	0.86	1.17	1.19	0.64

215 and the standard errors of the estimate (SEE) of linear regressions between  
 216 hvFE and experimental stiffness for pooled and single configurations. Femur-  
 217 specific fabric improved the correlations in pooled ( $p < 0.001$ ) and stance  
 218 configurations. The regression equations of the isotropic models, anisotropic  
 219 models with femur-specific fabric and anisotropic models with mean fabric  
 220 were  $y = 0.76x + 0.329$ ,  $y = 0.61x + 0.365$  and  $y = 0.62x + 0.547$ , respectively.  
 221 Examples of damage distribution at ultimate force in both stance and side-  
 222 fall configurations are shown in Fig. 3.

#### 223 4. Discussion

224 This study evaluates non-linear anisotropic QCT-based hvFE models of  
 225 the human proximal femur for the first time. The computed FE ultimate  
 226 force and stiffness of 71 femora in both stance and side-fall configurations

Table 3: **Prediction of stiffness.** Coefficients of determination  $r^2$  and standard errors of the estimate ( $SEE$ ) of the linear regressions of the relationships between hvFE and experimental stiffness in pooled stance and side-fall configurations, stance configuration and side-fall configuration. Comparison was made with previous studies on the same collection of femora.

	$r^2$			$SEE$ [kN]		
	pooled	stance	fall	pooled	stance	fall
<b>QCT</b> [12]						
Isotropic	0.90	0.82	0.74	0.88	0.91	0.23
<b>QCT</b> Present study						
Isotropic	0.90	0.82	0.79	0.89	1.35	0.21
Anisotropic: mean fabric	0.91	0.81	0.76	0.84	4.77	0.23
Anisotropic: femur-specific fabric	0.93	0.84	0.78	0.76	1.51	0.22
<b>HR-pQCT</b> [13]						
Anisotropic: femur-specific fabric	0.92	0.86	0.80	0.78	0.73	0.21

227 were compared with experimental results from Dall’Ara et al. [12]. The  
 228 set of femora has a broad spectrum of age and T-score, which supports the  
 229 generality of the findings. As expected, isotropic models of the current study  
 230 and those of Dall’Ara et al. [12] predict experimental ultimate forces similarly  
 231 (Table 2). The minor improvements of the correlation coefficients obtained  
 232 in the present study are most probably due to the more realistic reproduction  
 233 of the experimental boundary conditions.

234 Anisotropy significantly improves prediction ( $r^2$ ) of experimental ultimate  
 235 force in pooled configurations by 7 % for femur-specific fabric and 5 % for  
 236 mean fabric compared to isotropic models ( $r^2 = 0.81$ ). The small difference  
 237 between femur-specific and mean fabric confirms the ability of the mapping  
 238 algorithm to produce an approximate but realistic trabecular orientation in  
 239 the QCT-based FE models [46].

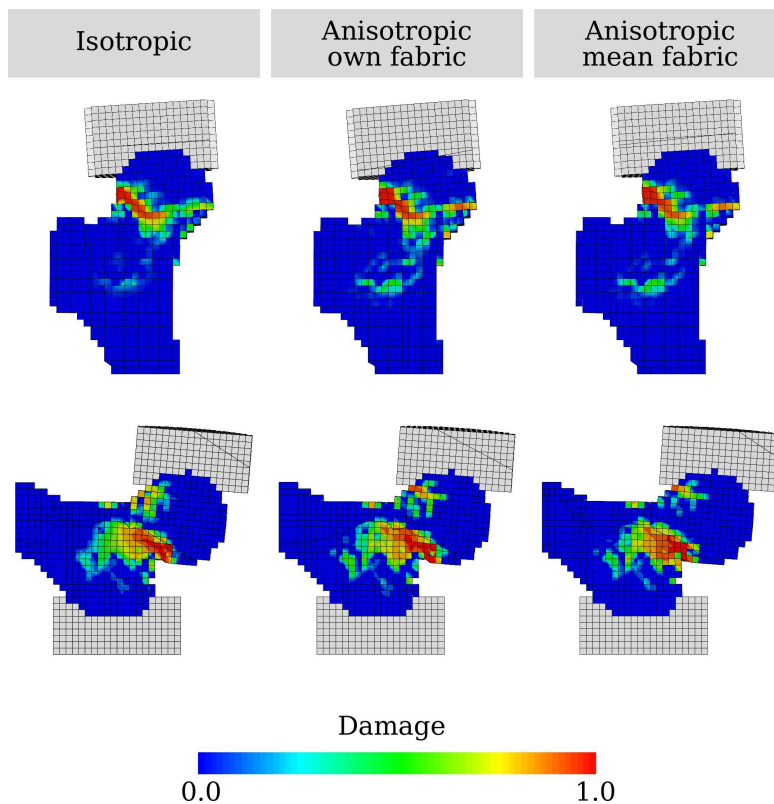


Figure 3: Damage at ultimate force obtained with the isotropic and anisotropic with femur-specific or mean fabric hvFE models.

240 Nevertheless, mean fabric enhances prediction of bone strength in pooled  
 241 configurations. This shows that HR-pQCT mean-fabric template could ben-  
 242 efit the hvFE analysis of the proximal femur in clinical CT images, where  
 243 the femur-specific fabric is not available. In the side-fall configuration, the  
 244 effect of anisotropy is negligible. This agrees well with the finding of [13]  
 245 and [14]. In fact, the stress distribution of the side-fall load configuration  
 246 does not align with the main compressive trabecular bundle of the proximal  
 247 femur and is therefore less sensitive to fabric. In addition, QCT-based hvFE

248 may simply not properly capture the architecture of the later cortex failing  
249 in compression in the fall configuration.

250 However, patients fall in various configurations. The validation for pooled  
251 configurations prevents over-fitting the FE models to a specific load configu-  
252 ration. As anisotropy helps align the regression lines of the two load configu-  
253 rations, it suggests that the methodology to generate anisotropic QCT-based  
254 FE models of the proximal femur is more general and could be valid for other  
255 clinically relevant load configurations.

256 Compared to published FE analyses of the proximal femur, the strength  
257 prediction ability of anisotropic hvFE models using femur-specific fabric is  
258 in the mid-range for pooled cases ( $r^2=0.80-0.94$ ) [28, 12, 13, 29, 5] and for  
259 stance cases ( $r^2=0.75-0.96$ ), and is in the upper range for side-fall cases  
260 ( $r^2=0.73-0.90$ ) [61, 19, 33]. In particular, these predictions are comparable  
261 to HR-pQCT-based homogenised smooth FE (hsFE) models of [13] which  
262 are slightly better in stance configuration (hvFE:  $r^2=0.84$ , hsFE:  $r^2=0.87$ )  
263 but equivalent in pooled and side-fall ( $r^2=0.86$ ) configurations.

264 The hvFE models of the current study explain more than 90 % of experi-  
265 mental bone stiffness for the pooled loading cases. In stance case, anisotropic  
266 models predict stiffness better than published FE models ( $r^2=0.62-0.82$ )  
267 [23, 12] and are in the mid-range for side-fall cases ( $r^2=0.72-0.87$ ) [14, 15, 33,  
268 17]. The results show that hvFE models overestimate experimental stiffness.  
269 However, the measured stiffness in biomechanical tests could be lower than  
270 the actual stiffness due to the presence of a compliant cartilage layer around

271 the femoral head in the experiments [12].

272 The results suggest also that hvFE models underestimate ultimate load.  
273 The anisotropic material constants of ultimate strength are taken from [62]  
274 and may indeed require a correction for the different *in situ* boundary con-  
275 ditions [63] associated with the loading of the whole proximal femur. The  
276 mesh size of 3 mm was shown to be a good compromise for hvFE models. On  
277 the one hand, this element size is larger than cortical thickness and smaller  
278 than the trabecular biopsies side-length of 5.3 mm used for homogenisation  
279 of elastic and yield properties by [49, 51]. Nevertheless, it provides a com-  
280 parable prediction to HR-pQCT-based homogenised, smooth finite element  
281 (hsFE) models.

282 We investigated the mesh convergence behaviour for stiffness by refining  
283 the isotropic hvFE models from 3 mm to 1.5 mm and 1 mm. The refer-  
284 ence images for the assignment of material properties remained identical to  
285 exclude the influence of material property mapping in the convergence anal-  
286 ysis. The stiffness difference between 3 mm and 1.5 mm meshes were 6.4 %,  
287 and between 1.5 mm and 1 mm meshes 1.6 %. This indicates that stiffness  
288 computed with 3 mm voxels remained within approximately 10% of the one  
289 calculated with a converged voxel mesh. Given the usual close relationship  
290 between FE stiffness and ultimate load, we expect this convergence behaviour  
291 for stiffness to remain in the same order of magnitude for ultimate load. Nev-  
292 ertheless, when considering anisotropic hvFE models with 1.5 mm mesh size,  
293 the regression curve between experimental and hvFE ultimate forces did not

294 match the 1:1 relationship. This may be due to other factors such as the dis-  
295 tinct representative volume element size in cortical and trabecular regions.  
296 In addition, mesh refinement (from 3 mm to 1.5 mm) did not improve pre-  
297 diction of anisotropic models in pooled configurations. This indicates that  
298 anisotropy dominates the reconciliation of the strength prediction between  
299 the stance and side-fall load cases.

300 In addition, the 3 mm models were cost-effective. They took only 7 GB  
301 memory and 20 minutes CPU time for a non-linear analysis which could be  
302 performed on a normal desktop PC. Finer meshes required a more powerful  
303 computing machine. The 1.5 mm mesh required 12 GB memory and 4 hours  
304 CPU time for a non-linear analysis. The 1 mm mesh took up to 50 GB  
305 memory and 5 hours for a single-step linear FE analysis.

306 There are some limitations in this study. First, the hvFE models gen-  
307 erated in this study are specific for the *in vitro* mechanical testing from  
308 Dall’Ara et al. [12]. QCT images of isolated proximal femora are not rigor-  
309 ously equivalent to QCT images of the same skeletal element *in vivo*. Second,  
310 due to the presence of the cartilage interface, the experimental setup led to  
311 lower measured stiffness compared to the simulated bone stiffness. Con-  
312 sequently, elastic properties of hvFE models cannot be validated properly.  
313 Third, the cortex surrounding the proximal femur cannot be properly rep-  
314 resented by 3 mm voxels. This limitation could be circumvented by using  
315 methods that were proposed to extract cortical thickness from QCT images  
316 [64, 65]. For accurate modelling of the cortical shell, smooth wedge elements

317 may be used [13]. Fourth, the RVE size for trabecular bone and cortical bone  
318 were identical. When trabecular and cortical layers could be modelled sepa-  
319 rately, different RVE size for each layer could be adjusted to achieve better  
320 predictions. Fifth, the mean femur template used to map anisotropy in this  
321 study is specific to the available collection of 71 femora and may need to  
322 be generalised to larger collections of femora in future clinical applications.  
323 Lastly, material properties were not fine-tuned but directly taken from [62].  
324 This was not the focus of this study but a proper tuning could obviously  
325 align prediction curve with the 1:1 relationship.

326 In this study, non-linear anisotropic QCT-based hvFE models of the prox-  
327 imal femur in pooled stance and side-fall configurations were validated for  
328 the first time. Anisotropy improves significantly bone strength and stiffness  
329 prediction in pooled configurations, and the prediction of mean-fabric tem-  
330 plate is comparable to femur-specific fabric. This suggests that mapping  
331 mean fabric-anisotropy could help generate QCT-based hvFE models of the  
332 proximal femur for clinical application. In future studies, the influence of  
333 the cortical layer in QCT-based hvFE needs to be investigated by modelling  
334 cortical and trabecular regions separately. This could be achieved by us-  
335 ing smooth wedge or shell elements of variable thickness. Additionally, a  
336 proper RVE size and material constants need to be defined for each com-  
337 partment. More accurate FE models are expected to enhance accuracy of  
338 femoral strength prediction and the associated fracture risk assessment.

339 **Acknowledgements** The authors would like to thank Dr. Vimal Chandran  
340 for providing the image registration methodology and Dr. Elham Taghizadeh  
341 for insightful discussion in fabric mapping. The simulations were performed  
342 on the Ubelix cluster of the University of Bern. This research was supported  
343 by grant no 143769 of the Swiss National Science Foundation.

344 **Declarations** The authors have no conflicts of interests.

345 **References**

- 346 [1] J. A. Kanis, O. Johnell, A. Oden, C. De Laet, B. Jonsson, A. Dawson,  
347 Ten-year risk of osteoporotic fracture and the effect of risk factors on  
348 screening strategies, *Bone* 30 (1) (2002) 251–258. doi:10.1016/S8756-  
349 3282(01)00653-6.
- 350 [2] S. C. E. Schuit, M. van der Klift, A. E. A. M. Weel, C. E. D. H. de Laet,  
351 H. Burger, E. Seeman, A. Hofman, A. G. Uitterlinden, J. P. T. M. van  
352 Leeuwen, H. A. P. Pols, Fracture incidence and association with bone  
353 mineral density in elderly men and women: the Rotterdam Study, *Bone*  
354 34 (1) (2004) 195–202. doi:10.1016/j.bone.2003.10.001.
- 355 [3] L. Langsetmo, D. Goltzman, C. S. Kovacs, J. D. Adachi, D. A. Hanley,  
356 N. Kreiger, R. Josse, A. Papaioannou, W. P. Olszynski, S. A. Jamal, Re-  
357 peat Low-Trauma Fractures Occur Frequently Among Men and Women  
358 Who Have Osteopenic BMD, *Journal of Bone and Mineral Research*  
359 24 (9) (2009) 1515–1522. doi:10.1359/jbmr.090319.
- 360 [4] D. L. Kopperdahl, T. Aspelund, P. F. Hoffmann, S. Sigurdsson,  
361 K. Siggeirsdottir, T. B. Harris, V. Gudnason, T. M. Keaveny, Assess-  
362 ment of Incident Spine and Hip Fractures in Women and Men using  
363 Finite Element Analysis of CT Scans, *Journal of bone and mineral re-  
364 search : the official journal of the American Society for Bone and Mineral  
365 Research* 29 (3) (2014) 570–580. doi:10.1002/jbmr.2069.

- 366 [5] P. Pottecher, K. Engelke, L. Duchemin, O. Museyko, T. Moser, D. Mit-  
367 ton, E. Vicaut, J. Adams, W. Skalli, J. D. Laredo, V. Bousson, Predic-  
368 tion of Hip Failure Load: In Vitro Study of 80 Femurs Using Three Imag-  
369 ing Methods and Finite Element ModelsThe European Fracture Study  
370 (EFFECT), *Radiology* (2016) 142796doi:10.1148/radiol.2016142796.
- 371 [6] J. Keyak, M. Fourkas, J. Meagher, H. Skinner, Validation of an auto-  
372 mated method of three-dimensional finite element modelling of bone.,  
373 *Journal of Biomedical Engineering* 15 (6) (1993) 505–9.
- 374 [7] B. Merz, P. Niederer, R. Muller, P. Ruegsegger, Automated finite ele-  
375 ment analysis of excised human femora based on precision -QCT., *Jour-  
376 nal of Biomechanical Engineering* 118 (3) (1996) 387–90.
- 377 [8] D. Cody, F. Hou, G. Divine, D. Fyhrie, Short term in vivo precision  
378 of proximal femoral finite element modeling.[Erratum appears in *Ann  
379 Biomed Eng* 2000 Nov-Dec;28(11):1397], *Annals of Biomedical Engi-  
380 neering* 28 (4) (2000) 408–14.
- 381 [9] T. M. Keaveny, P. F. Hoffmann, M. Singh, L. Palermo, J. P. Bilezikian,  
382 S. L. Greenspan, D. M. Black, Femoral Bone Strength and Its Relation  
383 to Cortical and Trabecular Changes After Treatment With PTH, Alen-  
384 dronate, and Their Combination as Assessed by Finite Element Analysis  
385 of Quantitative CT Scans, *Journal of Bone and Mineral Research* 23 (12)  
386 (2008) 1974–1982. doi:10.1359/jbmr.080805.

- 387 [10] L. Grassi, E. Schileo, F. Taddei, L. Zani, M. Juszczuk, L. Cristofolini,  
388 M. Viceconti, Accuracy of finite element predictions in sideways load  
389 configurations for the proximal human femur, *Journal of Biomechanics*  
390 45 (2) (2012) 394–399. doi:10.1016/j.jbiomech.2011.10.019.
- 391 [11] J. Hazrati Marangalou, K. Ito, B. van Rietbergen, A new approach to  
392 determine the accuracy of morphologyelasticity relationships in contin-  
393 uum FE analyses of human proximal femur, *Journal of Biomechanics*  
394 45 (16) (2012) 2884–2892. doi:10.1016/j.jbiomech.2012.08.022.
- 395 [12] E. Dall’Ara, B. Luisier, R. Schmidt, F. Kainberger, P. Zysset, D. Pahr,  
396 A nonlinear QCT-based finite element model validation study for the  
397 human femur tested in two configurations in vitro, *Bone* 52 (1) (2013)  
398 27–38. doi:10.1016/j.bone.2012.09.006.
- 399 [13] B. Luisier, E. DallAra, D. H. Pahr, Orthotropic HR-pQCT-based FE  
400 models improve strength predictions for stance but not for side-way fall  
401 loading compared to isotropic QCT-based FE models of human femurs,  
402 *Journal of the Mechanical Behavior of Biomedical Materials* 32 (2014)  
403 287–299. doi:10.1016/j.jmbbm.2014.01.006.
- 404 [14] W. S. Enns-Bray, J. S. Owoc, K. K. Nishiyama, S. K. Boyd, Map-  
405 ping anisotropy of the proximal femur for enhanced image based finite  
406 element analysis, *Journal of Biomechanics* 47 (13) (2014) 3272–3278.  
407 doi:10.1016/j.jbiomech.2014.08.020.

- 408 [15] W. S. Enns-Bray, O. Ariza, S. Gilchrist, R. P. Widmer Soyka, P. J. Vogt,  
409 H. Palsson, S. K. Boyd, P. Guy, P. A. Crompton, S. J. Ferguson, B. Helga-  
410 sson, Morphology based anisotropic finite element models of the proximal  
411 femur validated with experimental data, *Medical Engineering & Physics*  
412 38 (11) (2016) 1339–1347. doi:10.1016/j.medengphy.2016.08.010.
- 413 [16] M. Qasim, G. Farinella, J. Zhang, X. Li, L. Yang, R. Eastell, M. Vice-  
414 conti, Patient-specific finite element estimated femur strength as a pre-  
415 dictor of the risk of hip fracture: the effect of methodological deter-  
416 minants, *Osteoporosis International* (2016) 1–8doi:10.1007/s00198-016-  
417 3597-4.
- 418 [17] F. Johannesdottir, E. Thrall, J. Muller, T. M. Keaveny, D. L. Kopp-  
419 erdahl, M. L. Bouxsein, Comparison of non-invasive assessments of  
420 strength of the proximal femur, *Bone*doi:10.1016/j.bone.2017.07.023.
- 421 [18] K. Engelke, T. Lang, S. Khosla, L. Qin, P. Zysset, W. D. Leslie, J. A.  
422 Shepherd, J. T. Schousboe, Clinical Use of Quantitative Computed To-  
423 mography (QCT) of the Hip in the Management of Osteoporosis in  
424 Adults: the 2015 ISCD Official PositionsPart I, *Journal of Clinical Den-  
425 sitymetry* 18 (3) (2015) 338–358. doi:10.1016/j.jocd.2015.06.012.
- 426 [19] P. Zysset, L. Qin, T. Lang, S. Khosla, W. D. Leslie, J. A. Shepherd,  
427 J. T. Schousboe, K. Engelke, Clinical Use of Quantitative Computed  
428 TomographyBased Finite Element Analysis of the Hip and Spine in the

- 429 Management of Osteoporosis in Adults: the 2015 ISCD Official Posi-  
430 tionsPart II, *Journal of Clinical Densitometry* 18 (3) (2015) 359–392.  
431 doi:10.1016/j.jocd.2015.06.011.
- 432 [20] D. D. Cody, G. J. Gross, F. J. Hou, H. J. Spencer, S. A. Goldstein,  
433 D. P. Fyhrie, Femoral strength is better predicted by finite element  
434 models than QCT and DXA, *Journal of Biomechanics* 32 (10) (1999)  
435 1013–1020. doi:10.1016/S0021-9290(99)00099-8.
- 436 [21] J. Keyak, Improved prediction of proximal femoral fracture load using  
437 nonlinear finite element models, *Medical Engineering & Physics* 23 (3)  
438 (2001) 165–173. doi:10.1016/S1350-4533(01)00045-5.
- 439 [22] M. Bessho, I. Ohnishi, J. Matsuyama, T. Matsumoto, K. Imai, K. Naka-  
440 mura, Prediction of strength and strain of the proximal femur by a  
441 CT-based finite element method, *Journal of Biomechanics* 40 (8) (2007)  
442 1745–1753. doi:10.1016/j.jbiomech.2006.08.003.
- 443 [23] L. Duchemin, D. Mitton, E. Jolivet, V. Bousson, J. Laredo, W. Skalli, An  
444 anatomical subject-specific FE-model for hip fracture load prediction.,  
445 *Computer Methods in Biomechanics & Biomedical Engineering* 11 (2)  
446 (2008) 105–11.
- 447 [24] R. Hambli, E. Lespessailles, C.-L. Benhamou, Integrated remodeling-to-  
448 fracture finite element model of human proximal femur behavior, *Journal*

- 449 of the Mechanical Behavior of Biomedical Materials 17 (2013) 89–106.  
450 doi:10.1016/j.jmbbm.2012.08.011.
- 451 [25] D. Dragomir-Daescu, J. O. D. Buijs, S. McEligot, Y. Dai, R. C. En-  
452 twistle, C. Salas, L. J. M. Iii, K. E. Bennet, S. Khosla, S. Amin, Robust  
453 QCT/FEA Models of Proximal Femur Stiffness and Fracture Load Dur-  
454 ing a Sideways Fall on the Hip, *Annals of Biomedical Engineering* 39 (2)  
455 (2011) 742–755. doi:10.1007/s10439-010-0196-y.
- 456 [26] J. E. Koivumäki, J. Thevenot, P. Pulkkinen, V. Kuhn, T. M. Link,  
457 F. Eckstein, T. Jämsä, Ct-based finite element models can be used to  
458 estimate experimentally measured failure loads in the proximal femur,  
459 *Bone* 50 (4) (2012) 824–829. doi:10.1016/j.bone.2012.01.012.
- 460 [27] K. K. Nishiyama, S. Gilchrist, P. Guy, P. Cripton, S. K. Boyd, Proximal  
461 femur bone strength estimated by a computationally fast finite element  
462 analysis in a sideways fall configuration, *Journal of Biomechanics* 46 (7)  
463 (2013) 1231–1236. doi:10.1016/j.jbiomech.2013.02.025.
- 464 [28] J. H. Keyak, S. A. Rossi, K. A. Jones, H. B. Skinner, Prediction  
465 of femoral fracture load using automated finite element modeling,  
466 *Journal of Biomechanics* 31 (2) (1998) 125–133. doi:10.1016/S0021-  
467 9290(97)00123-1.
- 468 [29] E. Schileo, L. Balistreri, L. Grassi, L. Cristofolini, F. Taddei, To what  
469 extent can linear finite element models of human femora predict failure

- 470 under stance and fall loading configurations?, *Journal of Biomechanics*  
471 47 (14) (2014) 3531–3538. doi:10.1016/j.jbiomech.2014.08.024.
- 472 [30] T. Harrigan, M. Jasty, R. Mann, W. Harris, Limitations of the con-  
473 tinuum assumption in cancellous bone, *Journal of Biomechanics* 21 (4)  
474 (1988) 269–275.
- 475 [31] G. Maquer, S. N. Musy, J. Wandel, T. Gross, P. K. Zysset, Bone Volume  
476 Fraction and Fabric Anisotropy Are Better Determinants of Trabecular  
477 Bone Stiffness than Other Morphological Variables, *Journal of Bone and*  
478 *Mineral Research* (2015) n/a–n/a/doi:10.1002/jbmr.2437.
- 479 [32] S. N. Musy, G. Maquer, J. Panyasantisuk, J. Wandel, P. K. Zysset,  
480 Not only stiffness, but also yield strength of the trabecular structure  
481 determined by non-linear FE is best predicted by bone volume fraction  
482 and fabric tensor, *Journal of the Mechanical Behavior of Biomedical*  
483 *Materials* 65 (2017) 808–813. doi:10.1016/j.jmbbm.2016.10.004.
- 484 [33] B. Helgason, S. Gilchrist, O. Ariza, P. Vogt, W. Enns-Bray, R. P. Wid-  
485 mer, T. Fitze, H. Plsson, Y. Pauchard, P. Guy, S. J. Ferguson, P. A.  
486 Cripton, The influence of the modulusdensity relationship and the mate-  
487 rial mapping method on the simulated mechanical response of the prox-  
488 imal femur in side-ways fall loading configuration, *Medical Engineering*  
489 *& Physics* 38 (7) (2016) 679–689. doi:10.1016/j.medengphy.2016.03.006.
- 490 [34] Z. Tabor, R. Petryniak, Z. Lataa, T. Konopka, The potential of

- 491 multi-slice computed tomography based quantification of the structural  
492 anisotropy of vertebral trabecular bone, *Medical Engineering & Physics*  
493 35 (1) (2013) 7–15. doi:10.1016/j.medengphy.2012.03.003.
- 494 [35] M. E. Kersh, P. K. Zysset, D. H. Pahr, U. Wolfram, D. Larsson, M. G.  
495 Pandy, Measurement of structural anisotropy in femoral trabecular bone  
496 using clinical-resolution CT images, *Journal of Biomechanics* 46 (15)  
497 (2013) 2659–2666. doi:10.1016/j.jbiomech.2013.07.047.
- 498 [36] D. Larsson, B. Luisier, M. E. Kersh, E. Dall’ara, P. K. Zysset, M. G.  
499 Pandy, D. H. Pahr, Assessment of transverse isotropy in clinical-level  
500 ct images of trabecular bone using the gradient structure tensor, *Ann*  
501 *Biomed Eng* 42 (5) (2014) 950–9.
- 502 [37] D. H. Pahr, E. Dall’Ara, P. Varga, P. K. Zysset, HR-pQCT-based ho-  
503 mogenised finite element models provide quantitative predictions of ex-  
504 perimental vertebral body stiffness and strength with the same accuracy  
505 as FE models, *Computer Methods in Biomechanics and Biomedical En-*  
506 *gineering* 15 (7) (2012) 711–720. doi:10.1080/10255842.2011.556627.
- 507 [38] B. Van Rietbergen, A. Odgaard, J. Kabel, R. Huiskes, Direct me-  
508 chanics assessment of elastic symmetries and properties of trabecular  
509 bone architecture, *Journal of Biomechanics* 29 (12) (1996) 1653–1657.  
510 doi:10.1016/S0021-9290(96)80021-2.
- 511 [39] W. J. Whitehouse, The quantitative morphology of anisotropic

- 512 trabecular bone, *Journal of Microscopy* 101 (2) (1974) 153–168.  
513 doi:10.1111/j.1365-2818.1974.tb03878.x.
- 514 [40] T. P. Harrigan, R. W. Mann, Characterization of microstructural  
515 anisotropy in orthotropic materials using a second rank tensor, *Journal*  
516 *of Materials Science* 19 (3) (1984) 761–767. doi:10.1007/BF00540446.
- 517 [41] J. H. Marangalou, K. Ito, M. Cataldi, F. Taddei, B. v. Rietber-  
518 gen, A novel approach to estimate trabecular bone anisotropy using a  
519 database approach, *Journal of Biomechanics* 46 (14) (2013) 2356–2362.  
520 doi:10.1016/j.jbiomech.2013.07.042.
- 521 [42] K. Lekadir, C. Noble, J. Hazrati-Marangalou, C. Hoogendoorn, B. v.  
522 Rietbergen, Z. A. Taylor, A. F. Frangi, Patient-Specific Biomechan-  
523 ical Modeling of Bone Strength Using Statistically-Derived Fabric  
524 Tensors, *Annals of Biomedical Engineering* 44 (1) (2015) 234–246.  
525 doi:10.1007/s10439-015-1432-2.
- 526 [43] V. Chandran, P. K. Zysset, M. Reyes, Prediction of Trabecular Bone  
527 Anisotropy from Quantitative Computed Tomography Using Supervised  
528 Learning and a Novel Morphometric Feature Descriptor, in: N. Navab,  
529 J. Hornegger, W. M. Wells, A. F. Frangi (Eds.), *Medical Image Com-*  
530 *puting and Computer-Assisted Intervention – MICCAI 2015*, no. 9349 in  
531 *Lecture Notes in Computer Science*, Springer International Publishing,  
532 2015, pp. 621–628, dOI: 10.1007/978-3-319-24553-9\_76.

- 533 [44] E. Taghizadeh, M. Reyes, P. Zysset, A. Latypova, A. Terrier, P. Büchler,  
534 Biomechanical Role of Bone Anisotropy Estimated on Clinical CT Scans  
535 by Image Registration, *Annals of Biomedical Engineering* (2016) 1–  
536 13doi:10.1007/s10439-016-1551-4.
- 537 [45] E. Taghizadeh, V. Chandran, M. Reyes, P. Zysset, P. Büchler, Statisti-  
538 cal analysis of the inter-individual variations of the bone shape, volume  
539 fraction and fabric and their correlations in the proximal femur, *Bone*-  
540 doi:10.1016/j.bone.2017.07.012.
- 541 [46] V. Chandran, M. Reyes, P. Zysset, A novel registration-based method-  
542 ology for prediction of trabecular bone fabric from clinical qct: A com-  
543 prehensive analysis, *PLoS One* 12 (11).
- 544 [47] P. Zysset, D. Pahr, K. Engelke, H. K. Genant, M. R. McClung, D. L.  
545 Kandler, C. Recknor, M. Kinzl, J. Schwiedrzik, O. Museyko, A. Wang,  
546 C. Libanati, Comparison of proximal femur and vertebral body strength  
547 improvements in the freedom trial using an alternative finite element  
548 methodology, *Bone* 81 (2015) 122–130.
- 549 [48] S. Klein, M. Staring, K. Murphy, M. A. Viergever, J. P. W. Pluim,  
550 elastix: A Toolbox for Intensity-Based Medical Image Registra-  
551 tion, *IEEE Transactions on Medical Imaging* 29 (1) (2010) 196–205.  
552 doi:10.1109/TMI.2009.2035616.
- 553 [49] D. Pahr, P. Zysset, Influence of boundary conditions on computed ap-

- 554 parent elastic properties of cancellous bone., *Biomechanics & Modeling*  
555 in *Mechanobiology* 7 (6) (2008) 463–76.
- 556 [50] T. Gross, D. H. Pahr, P. K. Zysset, Morphology-elasticity relationships  
557 using decreasing fabric information of human trabecular bone from three  
558 major anatomical locations, *Biomechanics and modeling in mechanobi-*  
559 *ology* 12 (4) (2013) 793–800. doi:10.1007/s10237-012-0443-2.
- 560 [51] J. Panyasantisuk, D. H. Pahr, P. K. Zysset, Effect of boundary condi-  
561 tions on yield properties of human femoral trabecular bone, *Biomechan-*  
562 *ics and Modeling in Mechanobiology* (2015) 1–11doi:10.1007/s10237-  
563 015-0741-6.
- 564 [52] V. Chandran, P. Zysset, M. Reyes, Prediction of trabecular bone  
565 anisotropy from quantitative computed tomography using supervised  
566 learning and a novel morphometric feature descriptor, in: *Medical Im-*  
567 *age Computing and Computer-Assisted Intervention - Miccai 2015, Pt*  
568 *I, Vol. 9349, 2015, pp. 621–628.*
- 569 [53] M. Doube, M. M. Kosowski, I. Arganda-Carreras, F. P. Cordelires, R. P.  
570 Dougherty, J. S. Jackson, B. Schmid, J. R. Hutchinson, S. J. Shefelbine,  
571 *BoneJ: Free and extensible bone image analysis in ImageJ, Bone* 47 (6)  
572 (2010) 1076–1079. doi:10.1016/j.bone.2010.08.023.
- 573 [54] C. A. Schneider, W. S. Rasband, K. W. Eliceiri, *NIH Image to Im-*

- 574 ageJ: 25 years of image analysis, *Nature Methods* 9 (7) (2012) 671–675.  
575 doi:10.1038/nmeth.2089.
- 576 [55] D. Garcia, P. K. Zysset, M. Charlebois, A. Curnier, A three-dimensional  
577 elastic plastic damage constitutive law for bone tissue, *Biomechanics and*  
578 *Modeling in Mechanobiology* 8 (2) (2008) 149–165. doi:10.1007/s10237-  
579 008-0125-2.
- 580 [56] P. K. Zysset, A review of morphologyelasticity relationships in human  
581 trabecular bone: theories and experiments, *Journal of Biomechanics*  
582 36 (10) (2003) 1469–1485. doi:10.1016/S0021-9290(03)00128-3.
- 583 [57] P. Zysset, L. Rincón, An Alternative Fabric-based Yield and Failure  
584 Criterion for Trabecular Bone, in: P. G. A. Holzapfel, P. R. W. Ogden  
585 (Eds.), *Mechanics of Biological Tissue*, Springer Berlin Heidelberg, 2006,  
586 pp. 457–470.
- 587 [58] L. Rincón-Kohli, P. K. Zysset, Multi-axial mechanical properties of hu-  
588 man trabecular bone, *Biomechanics and Modeling in Mechanobiology*  
589 8 (3) (2008) 195–208. doi:10.1007/s10237-008-0128-z.
- 590 [59] D. H. Pahr, J. Schwiedrzik, E. Dall’Ara, P. K. Zysset, Clinical versus  
591 pre-clinical FE models for vertebral body strength predictions, *Journal*  
592 *of the Mechanical Behavior of Biomedical Materials* 33 (2014) 76–83.  
593 doi:10.1016/j.jmbbm.2012.11.018.

- 594 [60] J. H. Steiger, Tests for comparing elements of a correlation matrix.,  
595 Psychological bulletin 87 (2) (1980) 245.
- 596 [61] S. van den Munckhof, A. A. Zadpoor, How accurately can we  
597 predict the fracture load of the proximal femur using finite el-  
598 element models?, Clinical Biomechanics 29 (4) (2014) 373–380.  
599 doi:10.1016/j.clinbiomech.2013.12.018.
- 600 [62] L. Rincon-Kohli, P. K. Zysset, Multi-axial mechanical properties of hu-  
601 man trabecular bone, Biomechanics and Modeling in Mechanobiology  
602 8 (3) (2009) 195–208.
- 603 [63] P. Wili, G. Maquer, J. Panyasantisuk, P. K. Zysset, Estimation of the ef-  
604 fective yield properties of human trabecular bone using nonlinear micro-  
605 finite element analyses, Biomech Model Mechanobiol 16 (6) (2017) 1925–  
606 1936.
- 607 [64] G. M. Treece, A. H. Gee, Independent measurement of femoral cortical  
608 thickness and cortical bone density using clinical CT, Medical Image  
609 Analysis 20 (1) (2015) 249–264. doi:10.1016/j.media.2014.11.012.
- 610 [65] O. Museyko, B. Gerner, K. Engelke, Cortical Bone Thickness Estimation  
611 in CT Images: A Model-Based Approach Without Profile Fitting, in:  
612 Computational Methods and Clinical Applications for Spine Imaging,  
613 Springer International Publishing, 2016.